BRAIN. Broad Research in Artificial Intelligence and Neuroscience
e-ISSN: 2067-3957 | p-ISSN: 2068-0473
Covered in: Web of Science (ESCI); EBSCO; JERIH PLUS (hkdir.no); IndexCopernicus; Google Scholar; SHERPA/RoMEO; ArticleReach Direct; WorldCat; CrossRef; Peeref; Bridge of Knowledge (mostwiedzy.pl); abcdindex.com; Editage; Ingenta Connect Publication; OALib; scite.ai; Scholar9; Scientific and Technical Information Portal; FID Move; ADVANCED SCIENCES INDEX (European Science Evaluation Centre, neredataltics.org); ivySCI; exaly.com; Journal Selector Tool (letpub.com); Citefactor.org; fatcat!; ZDB catalogue; Catalogue SUDOC (abes.fr); OpenAlex; Wikidata; The ISSN Portal; Socolar; KVK-Volltitel (kit.edu)
2025, Volume 16, Issue 3, pages: 169-198
Submitted: April 13th, 2025 | *Accepted for publication:* August 23rd, 2025

Development and Validation of a Navigation System Based on a 3D Digital Magnetic Sensor and an NdFeB Magnet for Interlocking of Intramedullary Nails: A Step Toward Neuro-Orthopaedic Integration and Future AI-Enhanced Guidance

Iustin Zaieț
Departament: Department of Anatomy and Embryology, Iuliu Hatieganu University of Medicine and Pharmacy,400348, Cluj-Napoca, Romania. Zaiet.Iustin@umfcluj.ro, https://orcid.org/0009-0003-7338-9854

Romulus-Dan Nicoară*
Iuliu Hațieganu University of Medicine and Pharmacy, Cluj-Napoca, Romania / National Association for Health Psychology and Medical Psychology, Cluj-Napoca, Romania. daninicoara@yahoo.it, https://orcid.org/0009-0002-9979-0008

Carmen Bianca Crivii
Departament: Department of Anatomy and Embryology, Iuliu Hatieganu University of Medicine and Pharmacy, 400348 Cluj-Napoca, Romania.
bianca.crivii@umfcluj.ro, https://orcid.org/0000-0001-5275-5753

Dinu Iuliu Dumitrascu
Departament: Department of Anatomy and Embryology, Iuliu Hatieganu University of Medicine and Pharmacy, 400348 Cluj-Napoca, Romania. d.dumitrascu@yahoo.com, https://orcid.org/0000-0001-8042-1582

Alexandru Florin Badea
Departament: Department of Anatomy and Embryology, Iuliu Hatieganu University of Medicine and Pharmacy, 400348 Cluj-Napoca, Romania. afbadea84@gmail.com, https://orcid.org/0009-0009-8554-3138

Răzvan Crețeanu
Departament: Department of Anatomy and Embryology, Iuliu Hatieganu University of Medicine and Pharmacy, 400348 Cluj-Napoca, Romania. https://orcid.org/0009-0002-0681-0955

Adriana Gabriela Filip
Departament: Department of Anatomy and Embryology, Iuliu Hatieganu University of Medicine and Pharmacy, 400348 Cluj-Napoca, Romania. gabriela.filip@umfcluj.rom, https://orcid.org/0000-0002-7447-4925

** Corresponding author*

Abstract: *This study presents the Navigation Interlocking Magnetic System (NIMS), an innovative method for guiding distal locking screws in intramedullary osteosynthesis. Using a 3D digital magnetometer and a cylindrical NdFeB magnet, NIMS ensures precise alignment, significantly reducing operative time and eliminating radiation exposure. The system was rigorously tested, achieving an average procedural time of 21.24 seconds, with an average deviation of 1.541 mm and an angular error of 4.39 degrees. Although the results are promising, further improvements and additional clinical studies are needed to validate its efficiency in various orthopaedic applications. Due to these characteristics, NIMS represents a promising solution for optimising orthopaedic surgical interventions.Beyond its technical implementation, this work demonstrates an interdisciplinary strategy that connects clinical orthopaedics, computer science, and biomedical engineering. NIMS fits into the larger trend of intelligent surgical systems due to its combination of hardware components, real-time data processing, and procedural precision. Systems like NIMS may evolve into adaptive, artificial intelligence (AI)-driven platforms as artificial intelligence continues to influence intraoperative decision-making and surgical navigation, creating new opportunities for individualized and effective orthopedic care.*

Keywords: *magnetic sensor; intramedullary nail; permanent magnet (NdFeB); software simulation; magnetic field mapping robot (MFMR); navigation interlocking magnetic system (NIMS); AI (artificial intelligence).*

How to cite: Zaieț, I., Nicoară, R.-D., Crivii, C.B., Dumitrascu, D. I., Badea, A.F., Crețeanu, R., & Filip, A.G. (2025). Development and validation of a navigation system based on a 3D digital magnetic sensor and an NdFeB magnet for interlocking of intramedullary nails: A step toward neuro-orthopaedic integration and future AI-enhanced guidance. *BRAIN. Broad Research in Artificial Intelligence and Neuroscience*, 16(3), 169-198. https://doi.org/10.70594/brain/16.3/13

1. Introduction

Traditional methods for targeting distal locking holes in intramedullary nails, such as mechanical targeting systems and free-hand techniques, present notable limitations (Gao et al., 2021; Kelley et al., 1995; Knudsen, Grobler, & Close, 1991; Rahman, Taha, & Shaheen, 1998; Saw, 1993). Mechanical systems frequently fail due to nail deformation after insertion into the medullary canal, caused by the canal's anatomical characteristics and forces applied during insertion (Kelley et al., 1995; Knudsen, Grobler, & Close, 1991; Krettek et al., 1997). This deformation requires manual adjustments, increasing operative time. Although flexible, the free-hand method, is associated with high radiation exposure for patients and medical staff due to the frequent use of fluoroscopy to verify screw positions (Chung et al., 2012; Finelli et al., 2014; Gao et al., 2021; Leloup et al., 2008). Additionally, the accuracy of these methods is limited by the lack of precise and immediate feedback, potentially leading to incorrect implant placement. Various mechanical and electronic devices have been developed to optimise distal targeting, employing radiological exposures, laser technologies, or magnetic waves, but each presents specific limitations (Chabihi et al., 2024; Choi et al., 2017; Gao et al., 2021; Maleki et al., 2021; Wong et al., 2017; Xu, An, & Ko, 2021).

Laser technologies offer precision but face challenges related to variability in laser beam reflectance and absorption across different tissues, leading to poor control of the drilling angle and potential eye hazards for the user (Maleki et al., 2021; Xu et al., 2021). Electromagnetic targeting systems provide a non-invasive alternative, however they are susceptible to magnetic interference, which may introduce noise and errors in measurements (Antonini et al., 2016; Gao et al., 2021; Wang et al., 2018). However, rigorous calibration can significantly mitigate these disadvantages, allowing for adjustments to compensate for external influences and improving measurement accuracy and stability. Proper calibration helps manage magnetic interference effectively, enhancing the reliability and performance of these systems in surgical environments.

This paper outlines the development workflow of an innovative, cost-effective system utilising magnetic principles to provide a precise and reliable solution for distal targeting of intramedullary osteosynthesis. The Navigation Interlocking Magnetic System (NIMS) integrates a 3D digital magnetometer sensor *(MLX90392, MELEXIS, Ieper, Belgium)* (Melexis, 2024) and a permanent NdFeB cylindrical magnet *(N52, Asia Magnets Co. Ltd.)* to accurately detect the position of distal locking holes (DLHs). The magnetic data collected by the sensor are processed by an Arduino Uno microcontroller (Badamasi, 2014; D'Ausilio, 2012), and subsequently transmitted to a PC for assessment. An interactive graphical interface was developed to provide dynamic visualisation using NIMS, featuring visual representations of the magnet's position relative to the sensor, enabling precise navigation and stable alignment with the DLH, with the potential to use AI-based predictive models to improve more accurate trajectory.

The MLX90392 sensor was selected for its high precision in detecting magnetic fields in three-dimensional space and its compact size, which allows for integration into a probe that can be inserted into the nail. The NdFeB cylindrical magnet, with its high magnetic strength and stability, ensures optimal interaction with the sensor, even at greater distances, crucial for preventing device-patient collisions during surgery.

Commercial electromagnetic targeting devices require the surgeon to manually maintain the magnetic generator, which can compromise accuracy due to unintended hand movements during trans-osseous drilling (Antonini et al., 2016; Wang et al., 2018). In order to address this limitation, NIMS is equipped with a locking alignment frame that secures the magnetic element in the optimal position before drilling, eliminating the need for manual handling.

For the purpose of integrating sensors and magnets in a surgical simulation environment, a custom mounting frame was developed for a commercial nail model, with components designed using Free CAD v0.21.1, an open-source parametric 3D CAD software known for its flexibility and precision (Machado, Malpica, & Borromeo, 2019), and manufactured through 3D printing from Acrylonitrile Butadiene Styrene(ABS).Detailed analysis led to the selection of a cylindrical magnet with optimal characteristics for sensor interaction. Following the approach described by Smith, Johnson, & Lee (2022), a Cartesian robotic platform was developed to systematically map the magnetic field, thereby assisting in determining the optimal magnet dimensions and enabling automated data acquisition during sensor calibration - a process that may be further refined through machine learning-based calibration methods.

To evaluate NIMS's performance and reliability, practical tests were conducted under controlled conditions simulating real scenarios, focusing on measuring rotational and translational displacements and procedure time. The results demonstrate the device's potential to streamline the distal locking process of intramedullary nails, reducing procedure time and enhancing precision and efficiency. The main advantages of this system include its radiation-free technology and the provision of real-time three-dimensional feedback on position and orientation during drilling and fixation procedures for distal locking screws of intramedullary nails.

Orthopaedic surgery's intraoperative navigation and implant placement may benefit substantially from recent developments in artificial intelligence (AI). To deliver intraoperative feedback, predict ideal drilling trajectories, and minimise placement deviations during distal screw fixation, AI systems are becoming increasingly able to process multimodal intraoperative data in real time (Baghbani et al., 2025; Zhou et al., 2023). AI-driven algorithms could be incorporated into the NIMS system, which uses magnetic field mapping to determine the location of distal locking holes, to interpret fluctuating magnetic signals, identify interference patterns, and recommend dynamic alignment adjustments (Frontiers in Surgery, 2023; Gao et al., 2021). Additionally, NIMS may provide patient-specific navigation support through machine learning models based on anatomical variability, increasing its flexibility and accuracy in diverse clinical scenarios (Fauser et al., 2022). These improvements could turn NIMS from a passive targeting system into a semi-autonomous, intelligent platform that can support intraoperative decision-making in real time.

2. Materials and Methods

2.1. Integration of the Magnetic Sensor

The triaxial magnetometer sensor MLX90392 (Melexis) was used in the development of the prototype. Its remarkable features, based on Hall Triaxis™ technology, make it ideal for position sensor applications (Melexis, 2024). This sensor is notable for its compact dimensions (2 × 2.5 × 0.4 mm^3), allowing for easy integration inside a sample that can be inserted into the channel of an intramedullary rod. The sensor's compatibility with I^2C protocol and the digital output that includes 16-bit data for both magnetic measurements (XYZ) and ambient temperature, offers exceptional precision and versatility. The selectable operating modes during operation, such as Single Measurements or Continuous Mode with a rate of up to 1.4kHz for XYZ, allow flexible adaptation to the specific needs of the current experiment. To integrate the sensor, a structured process was implemented in two essential stages: hardware integration and software integration.

2.1.1. Hardware Integration

An initial detailed evaluation of the dimensions and shape of a commercial intramedullary nail was conducted to identify the optimal locations for the sensor placement. It was deemed necessary to insert the sensor into a probe compatible with the nail's canal, which has a diameter of 4 mm. To meet these requirements, a meticulous approach was adopted, involving the use of a Polytetrafluoroethylene (PTFE) tube with an outer diameter of 3 mm and an inner diameter of 2 mm as a protective and guiding support for the sensor. To reduce the tube's mobility within the nail's canal and facilitate its sliding, a 30 mm long PCB with a width extending to 3.6 mm at the end of the PTFE tube was created to accommodate the sensor. A visible mark was placed on the PTFE tube's surface to align with the centre of the sensor (Figure 1).

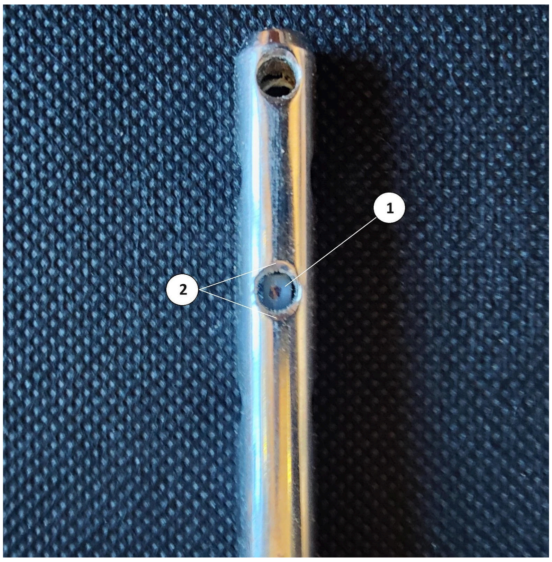

Figure 1.The PTFE tube inserted into the intramedullary nail. The sensor marking (1) is visible through the distal hole (2)

To ensure spatial integration of the sensor with the intramedullary nail and to facilitate its stability within the nail's canal, a dedicated clamp was constructed (Figure 2).

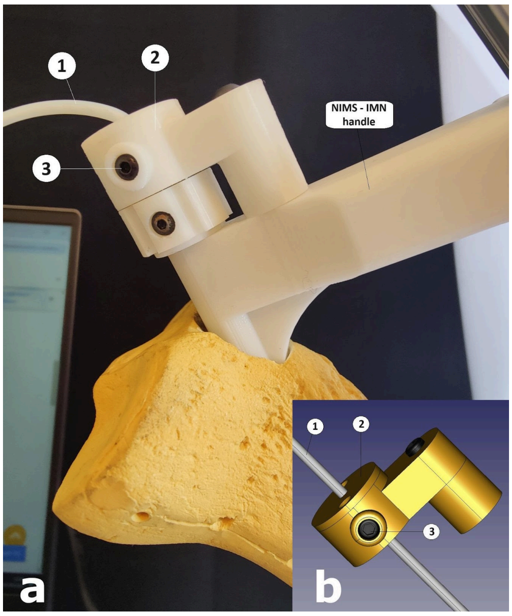

Figure 2. Clamp for securing the Teflon tube in position, obtained through 3D printing. The design was created using FreeCAD. 1.PTFE tube. 2.Clamp. 3. Screw for securing the clamp

The PTFE tube is secured in place on the clamp with two screws, and the clamp is attached to the nail insertion handle with another screw.

The insertion handle was designed to secure the clamp with a screw while also allowing a 20x20 mm aluminium V-slot profile piece to slide, enabling the system to adjust for nails of varying lengths (see Figure 3).

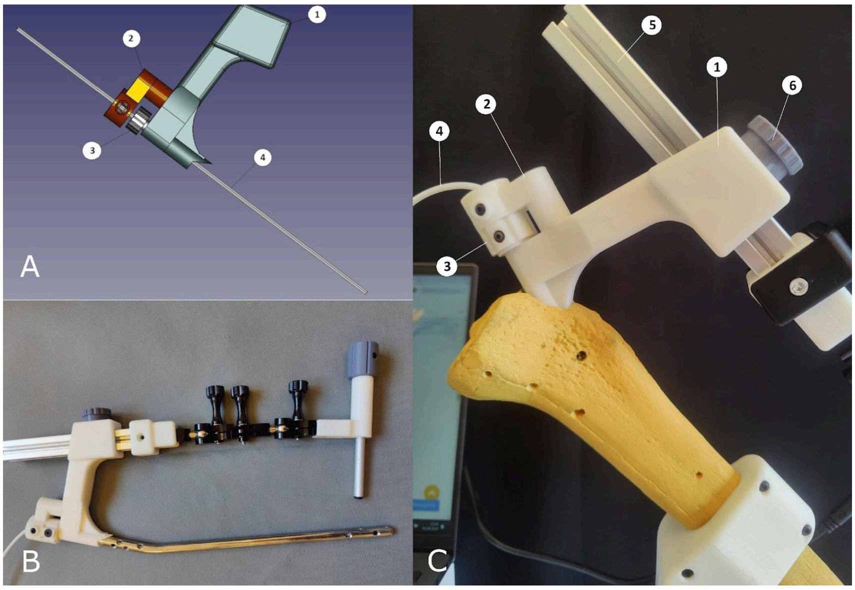

Figure 3. Nail handle designed to facilitate the attachment of other parts: 1. Nail handle, serving as the central element; 2. PTFE clamp, which secures the PTFE tube; 3. Handle screw, used to fix the nail; 4. PTFE tube with a sensor inside; 5. V-slot profile, allowing for adjustable positioning; 6. Locking button, securing the V-slot profile in place. The design was created using FreeCAD, and all components were 3D printed using an Ender3 v.3 printer with an enclosure, utilizing ABS material

Additionally, the handle features a screw mechanism that locks the V-slot profile in position. At the distal end of the V-slot profile, a coupling was added to attach a set of aluminium joints typically used for stabilising cameras, highlighting the need for an adjustable and lockable system. At the end of this assembly, a detachable mechanism was necessary to facilitate the interchangeable use of the magnetic probe guide with the probe used during the accuracy evaluation phase. The system was designed to allow precise attachment by aligning the necessary component and securing it using a screw.

2.1.2. Software Integration and Sensor Calibration Software Integration

To collect and process data from the MLX90392 sensor, it was essential to connect it to a microcontroller. An Arduino UNO board was selected as the control unit and interface due to its compatibility and flexibility. The developed software was configured to communicate with the sensor via the I2C bus, performing continuous magnetic field measurements on the X, Y, and Z axes. The algorithm initiates I2C communication and configures the sensor for continuous measurements, setting the sampling rate and activating a digital filter to optimise data accuracy. To reduce measurement noise, a moving average filter is applied by cyclically storing measured values in separate arrays for each axis. This method reduces the impact of sudden variations and noise, providing stabilised average values that more accurately reflect the observed magnetic field.

Sensor Calibration

Calibrating the MLX90392 sensor was essential to ensure precise and repeatable measurements. A Helmholtz coil with a diameter of 30 cm and 500 turns per coil, powered by a constant current of 1 A, was used for this purpose. The sensor was positioned at the centre of the coil, where the magnetic field is most uniform. The calibration process began by measuring the magnetic field values in the absence of any current applied to the coils to identify and correct any sensor offsets. Subsequently, a standardised current was applied, generating a magnetic field of 0.0001 Tesla, measured with a reference magnetometer. The sensor was calibrated to reflect these precise values by adjusting its internal parameters via firmware. The calibration results were significant, improving the sensor's measurement repeatability by reducing the standard deviation by

50% compared to initial measurements. Repeated test series under various laboratory conditions confirmed the reliability and effectiveness of the calibration process.

To calibrate the MLX90392 sensor for hard iron effects, raw magnetic field data were collected by rotating the sensor in all directions to capture a comprehensive set of measurements (Andel et al., 2022). The offset values for each axis were then calculated by averaging the maximum and minimum readings and subtracting these offsets from the measured values to centre the data around the origin. This process was implemented on the Arduino UNO platform, where sensor readings were taken and the offset values were computed and stored.

For soft iron calibration, a more complex approach was applied. Subsequent to hard-iron compensation, the covariance matrix of the centred data was calculated to understand the distortion characteristics. Using eigenvalue decomposition, a transformation matrix was derived that normalised the measured values, converting the measurement ellipsoid into a sphere. This transformation matrix was applied to the adjusted data to correct for distortions caused by nearby ferromagnetic materials.

On the Arduino UNO, the calibration process involved collecting a series of magnetic field measurements, computing the necessary offsets and transformation parameters, and applying these corrections in realtime during subsequent sensor operations. The result was a set of calibrated magnetic field values that accurately reflected the true magnetic field, free from distortions caused by both hard and soft iron effects.

While the current calibration procedures have proven effective, new research shows that artificial intelligence algorithms have the ability to improve sensor performance. Both hard and soft iron effects can be automatically corrected in a variety of clinical settings thanks to machine learning models that can identify distortion patterns in massive datasets. It has been demonstrated that neural networks, in particular, can detect minute nonlinearities and adaptively adjust sensors without the need for direct human assistance. With less reliance on laboratory calibration and more accurate intraoperative guidance in a variety of surgical settings, such an AI-driven approach could further strengthen the NIMS system's resilience (Belalcazar-Bolaños, Torricelli, & Pons, 2023; Christensen, Krell, & Kirchner, 2017; Xiao et al., 2025; Halitim & Bouhedda, 2024).

2.2. The Magnet Integration

2.2.1. Magnet Selection Process

The process of selecting the ideal magnet involved a detailed analysis of the interaction between the sensor and several neodymium (NdFeB) magnets, considering variables such as size and magnetic strength. Detailed analysis of the mechanical distal targeting system accessories showed that the diameter of the protection sleeves ranges between 8 and 10 mm, and the drill sleeves between 6 and 8 mm. To facilitate the use of standard commercial accessories, NdFeB N52 magnets with a diameter of 6 mm and variable lengths between 25 and 100 mm were used.

A 6 mm diameter was chosen to allow the magnet to be inserted into a 135 mm long aluminium tube with an 8 mm outer diameter and a 6.1 mm inner diameter, which can easily slide within the protective sleeve and serves as a magnetic probe. To improve usability, a 3D-printed handle was added to the magnetic probe (Figure 4).

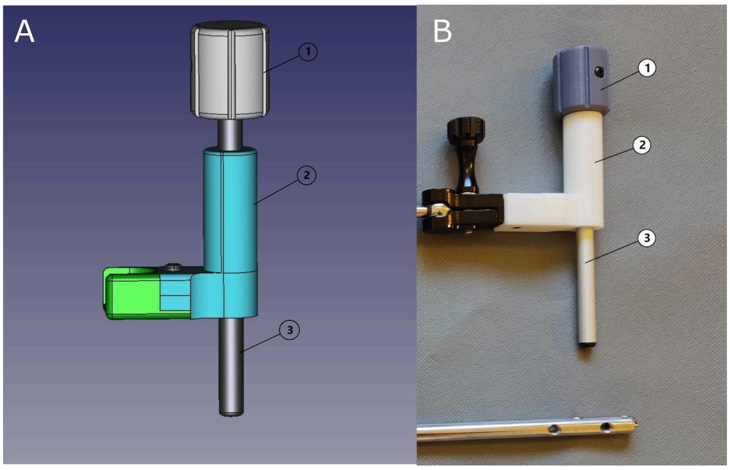

Figure 4. The design of the magnetic probe. A. freeCAD assembly model; B. Magnetic probe integrated with NIMS. 1.Probe handle; 2. NIMS probe sleeve; 3. Aluminium tube containing the magnet.

The choice of the N52 grade was essential due to its exceptional magnetic properties, including a high maximum magnetic energy (BHmax), ensuring optimal interaction with the sensor even at greater distances. This characteristic was crucial for developing the navigation system, where detection precision and reliability are imperative.

In this context, detailed magnetic field simulations were performed to evaluate different magnet sizes and identify the optimal configuration for the sensor at a target distance of at least 50 mm.

Radiographs from a cohort of patients with tibial fracture nails were analysed. This analysis quantified the distance between the tip of the nail and the transverse plane tangent to the articular surface of the distal tibia. An interval between 10 and 35 mm was obtained, which likely varies depending on the fracture configuration. In the case of a more distal fracture, the distance from the nail tip to the tibial articular surface decreases. For most of the nails analysed, the distance between the end of the nail and the most proximal hole in the distal end is 40 mm.

Based on these measurements, an area of interest was established, representing the working space, located between the distal tibial articular surface and a parallel plane 80 mm away through the tibial diaphysis. Within this area of interest, using axial CT sections obtained from a cohort of 35 patients, the farthest point from the centre of the bone to the skin was measured along the X and Y axes by image analysis using Fiji - ImageJ (Schindelin et al., 2012) (Figure 5).

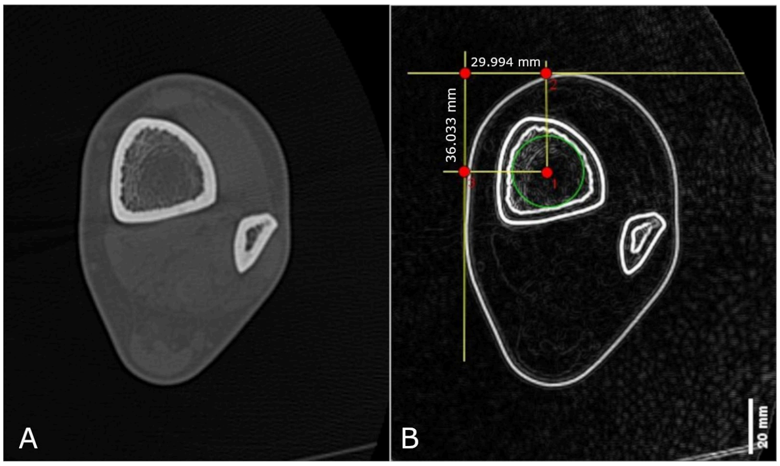

Figure 5. Figure 5. A. CT axial section image of the lower leg located 10mm from the articular surface of the distal tibial epiphysis. B. Image processed with ImageJ, using the "find edges" function to highlight the edges of interest. The green circle delineates the medullary canal, and distances were measured from its center to the maximum points on the X and Y axes

The greatest distances were observed in the transverse plane closest to the articular surface, located 10 mm proximally. Identifying these points is essential to prevent the device from colliding with the patient's limb (Table 1).

Table 1. The distances on the X and Y axes measured in the plane located 10 mm away from the articular surface of the distal tibia on axial CT images of a group of 35 cases with varied age and body weight

Case number	X value (mm)	Y value (mm)
1	30.232	29.454
2	35.425	34.22
3	35.121	34.47
4	28.414	27.235
5	27.242	27.114
6	40.102	39.425
7	44.254	43.321
8	30.123	29.356
9	38.245	37.845
10	45.623	44.862
11	29.212	28.322
12	28.878	27.411
13	32.366	31.98
14	41.125	40.745
15	36.363	35.547
16	34.798	34.499
17	40.252	40.119
18	39.253	39.147
19	39.455	39.324
20	31.247	30.478
21	33.5	30.74
22	46.77	44.789
23	48.99	49.012
24	35.645	34.987
25	38.798	37.41
26	34.455	33.144
27	36.741	35.642
28	40.95	39.147
29	41.44	40.144
30	42.221	40.98
31	31.235	28.74
32	30.956	29.877
33	32.123	30.654
34	33.424	32.95
35	34.245	33.147

To better understand the distribution and characteristics of the X and Y values, a statistical analysis was conducted. The X values have an average of approximately 35.69 mm and a median of 35.64 mm, indicating a relatively symmetrical distribution. The standard deviation was 5.33 mm, showing moderate variation. The minimum and maximum X values were 27.24 mm and 48.99 mm, respectively, with an interquartile range (IQR) of 7.73 mm, suggesting dispersion around the median. The maximum value of 48.99 mm is notably higher than the rest, indicating a potential outlier that requires careful consideration when placing the magnet.

The Y values have an average of 34.91 mm and a median of 34.69 mm, also indicating a relatively symmetrical distribution. The standard deviation is 5.61 mm, reflecting moderate variation. The minimum and maximum values for Y are 27.11 mm and 49.01 mm, respectively, with an IQR of 7.23 mm, indicating dispersion around the median. Similar to the X values, the maximum value of 49.01 mm is significant and must be considered when determining the magnet's placement relative to the sensor.

The analysis revealed that the X and Y values are symmetrically distributed with moderate variation, suggesting consistent measurements that well represent the studied population. Box plots (Figure 6) show the distribution of values and highlight outliers. The importance of the maximum values in both data sets cannot be underestimated, as they may represent critical or exceptional conditions that must be managed.

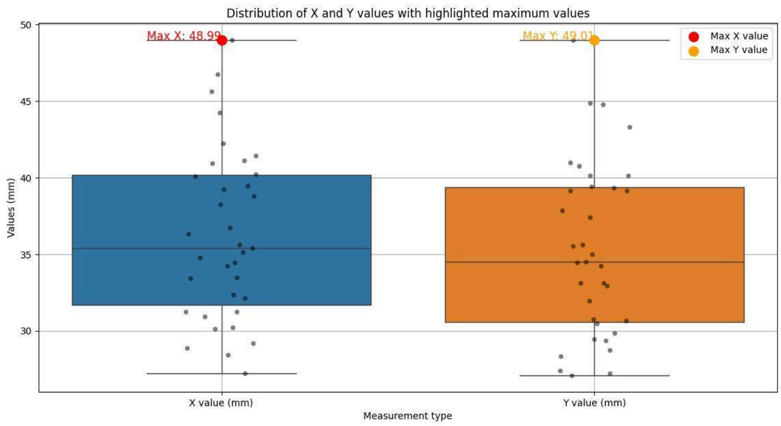

Figure 6. Distribution of Measured Values on the X and Y Axes

2.2.2. Simulation Processes

The magnetic field generated by a uniformly magnetised cylindrical magnet along its longitudinal axis can be mathematically described by integrating the magnetic field contributions of all volume elements of the magnet (Ravaud et al., 2010; Xu et al., 2021). For a point on the magnet's longitudinal axis, the magnetic field B(z) can be approximated by the following relation:

$$B(z) = \frac{\mu_0 M}{2}\left(\frac{z}{\sqrt{z^2+R^2}} - \frac{z-L}{\sqrt{(z-L)^2+R^2}}\right)$$

where μ_0 is the magnetic permeability of vacuum, M is the magnetisation of the magnet, L is the magnet length, R is the magnet radius, and z is the distance along the longitudinal axis from one end of the magnet. This formula accounts for the contributions of the magnetic field from both ends of the magnet and the rapid decrease in magnetic field intensity with distance from the magnet. It is derived by integrating the Biot-Savart law for a volume distribution of equivalent magnetic currents, considering the specific geometry of the cylindrical magnet (Ravaud et al., 2010; Xu et al., 2021).

To validate this theory and visualise the magnetic field distribution generated by cylindrical neodymium magnets, a complex workflow using specialised software tools was implemented. Initially, mesh models of the magnets were created using Salome, an open-source pre-processing software for finite element analysis (Nunio & Manil, 2012). These meshes were then used in Elmer, a multiphysics simulation open source software, to simulate the magnetic field behaviour (Keränen et al., 2015). The Solver Input File (SIF) generated by Elmer was used to run the magnetic simulations, and the raw magnetic field data were analysed and visualised in ParaView, a scientific visualisation software (Su et al., 2022).

Using ParaView, the magnetic field variations in different regions of the magnet were observed, and images and graphs illustrating these variations were generated. This combined workflow provided a detailed understanding of the magnetic field behavior and allowed for a visually attractive and easy-to-interpret presentation of the results.

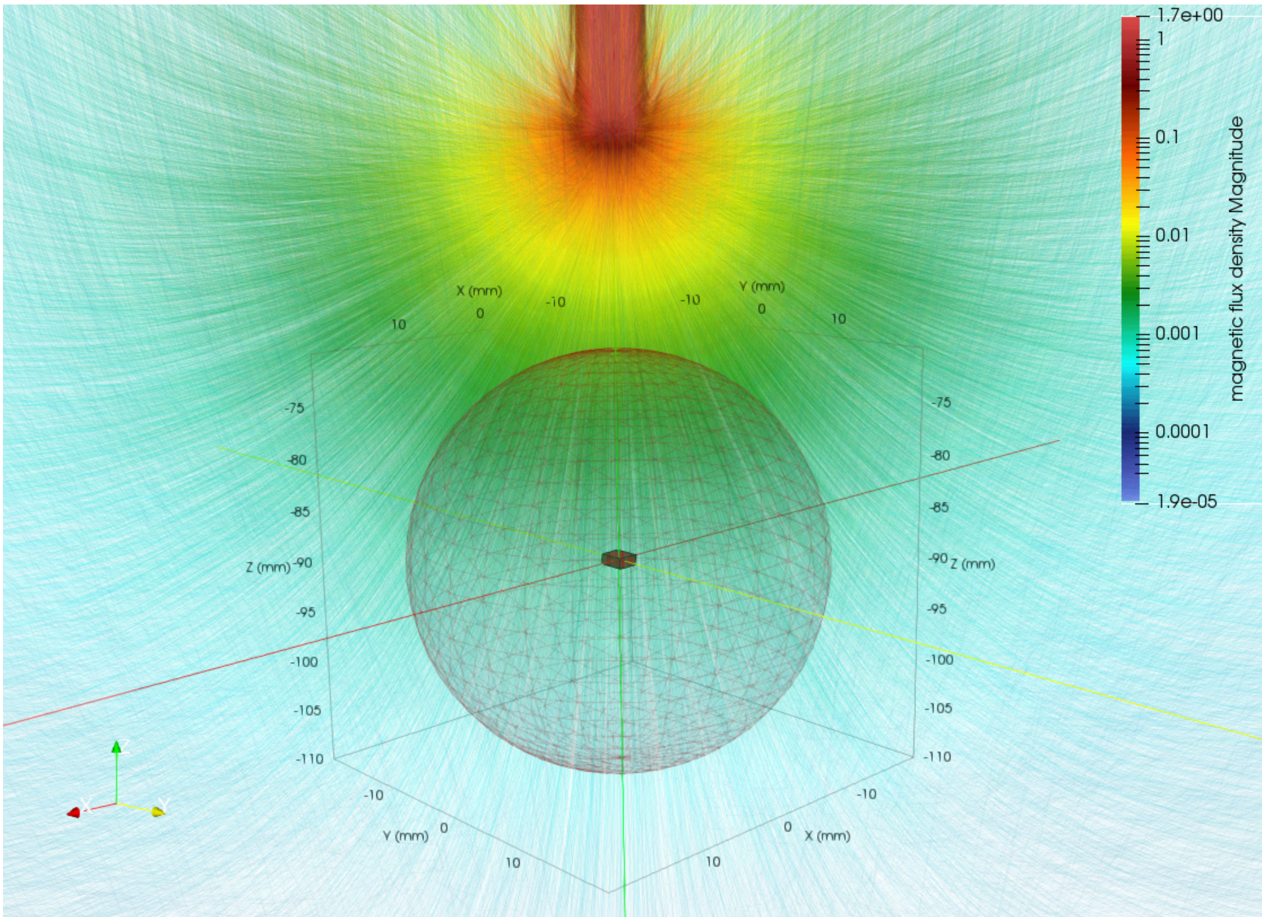

Figure 7. Visualization of the magnetic field generated by a cylindrical magnet using ParaView. The magnetic flux density is represented using color coding, and the the domain of analysis is illustrated by a sphere to indicate the analyzed area of interest

Figure 7 highlights the magnetic flux variation generated by a cylindrical *NdFeB N52* magnet, with a diameter of 6 mm and a length of 100 mm, and its density in the working space centered at a distance of 50 mm from the magnetic pole. The sensor is represented as a box with dimensions of 2 x 2.5 x 0.4 mm positioned at the centre of the working space *(Figure 7)*.

To further ensure the accuracy of the results, additional simulations were performed using Finite Element Method Magnetics (FEMM) version 4.2 (Meeker, 2024). These simulations included magnets with circular cross-sections of 6 mm diameter and lengths of 25 mm, 50 mm, 75 mm, and 100 mm *(Figure 8)*. Measurement points were placed at a fixed distance of 50 mm from the magnet's end to ensure data consistency. The mesh was refined in the critical region to accurately capture magnetic field variations.

September 2025
Volume 16, Issue 3

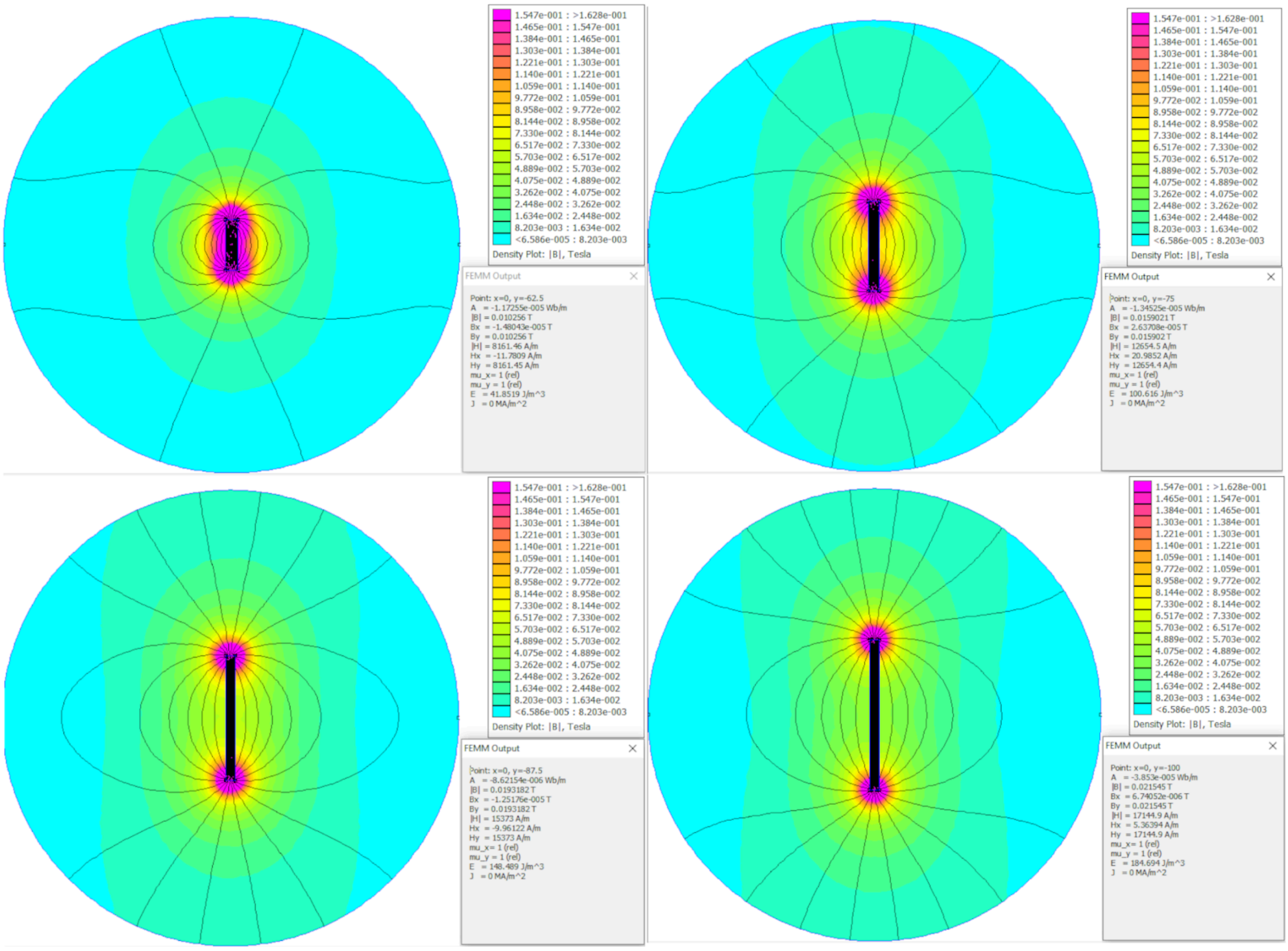

Figure 8. The distribution of the magnetic flux generated by cylindrical neodymium magnets

Figure 8 one can see the distribution of the magnetic flux generated by cylindrical neodymium magnets of grade N52 with a diameter of 6 mm and different lengths, simulated in FEMM: (**A**) 25 mm, (**B**) 50 mm, (**C**) 75 mm, (**D**) 100 mm. The colors indicate the magnetic flux density, from violet (maximum density) to light blue (minimum density). The measurement point was placed at a distance of -50 mm from the end of the magnet.

The results indicated an aproximately linear increase in magnetic field magnitude (|B|) with increasing magnet length *(Figure 8)*. This trend can be attributed to the larger amount of magnetic material contributing to the total field in longer magnets. However, the |B| values for each length did not follow perfect linearity, indicating the presence of edge effects and complex interactions between the magnetic poles.

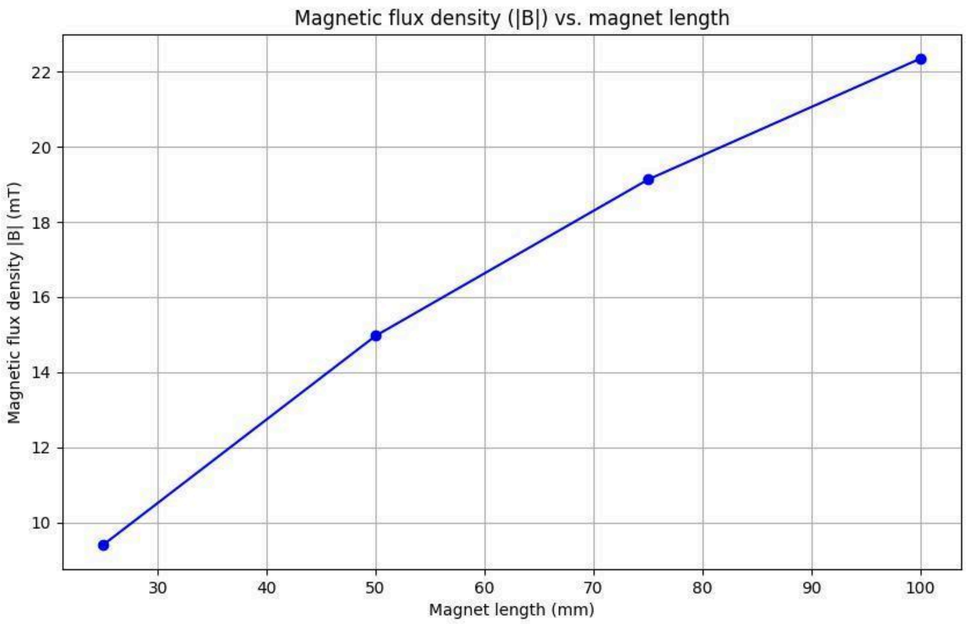

Figure 9. Variation of the magnetic field magnitude

In Figure 9 one can see the variation of the magnetic field magnitude (|B|) with length for cylindrical NdFeB N52 magnets with a diameter of 6mm. The length of the magnet varies between 25 mm and 100 mm. Magnetic field values are expressed in mT.

The results from the FEMM simulation help figure out the best size for magnets used in various situations, based on what the magnetic field needs to be. New developments in artificial intelligence show that machine learning can speed up finite element simulations and improve how we choose parameters in designing electromagnetic systems (Karniadakis et al., 2021; Bock et al., 2019). The selection of a 6 mm diameter facilitates the integration of the magnet, allowing it to be slid through the protective sleeve that holds the drill sleeve in a distal targeting system of an IMN. This setup makes sure that the system can adjust and work well in different medical situations, while also keeping the safety rules for locking the ends of intramedullary nails in broken tibia bones.

2.2.3. Experimental Magnetic Data Collection

After completing virtual simulations of the magnetic field for different magnet sizes and determining the optimal magnet length, the next step was to validate the results through physical experiments. To facilitate precise reading and data collection from the sensor, a Magnetic Field Mapping Robot (MFMR) was developed (Figure 9). This Cartesian robot, equipped with NEMA11 stepper motors with linear transmission, is controlled by an Arduino MEGA 2560 board, which communicates via a serial port with an Arduino UNO connected to the magnetic sensor. *A RAMPS 1.4* shield facilitated the addition of an LCD display with a control panel and SD card reader, thereby enhancing the prototype's functionality. The control panel, based on a rotary encoder, permitted precise manual adjustment of motor positions.

The MFMR frame was constructed from aluminium V-slot profiles and other mechanical components fabricated through 3D printing. The frame design was intended to accommodate the workspace requirements efficiently. Special attention was given to establishing a precise reference point to align the sensor's center with the magnet's centre in the X and Y coordinates, ensuring optimal horizontal and vertical alignment. This is crucial for precise measurements, as it ensures the magnetic field is evaluated directly along its maximum influence line.

A sensor holder and a specific magnet holder were developed, positioned at the end of the mapping system, contributing to establishing an exact reference point in the X, Y, and Z coordinates.

Non-magnetic materials were used for components like the sensor wiring and assembly parts to reduce magnetic interference. A minimum distance of 40 mm between the sensor and magnet was set when the MFMR's Z-axis was in its home position, determined by mechanical end-stops.

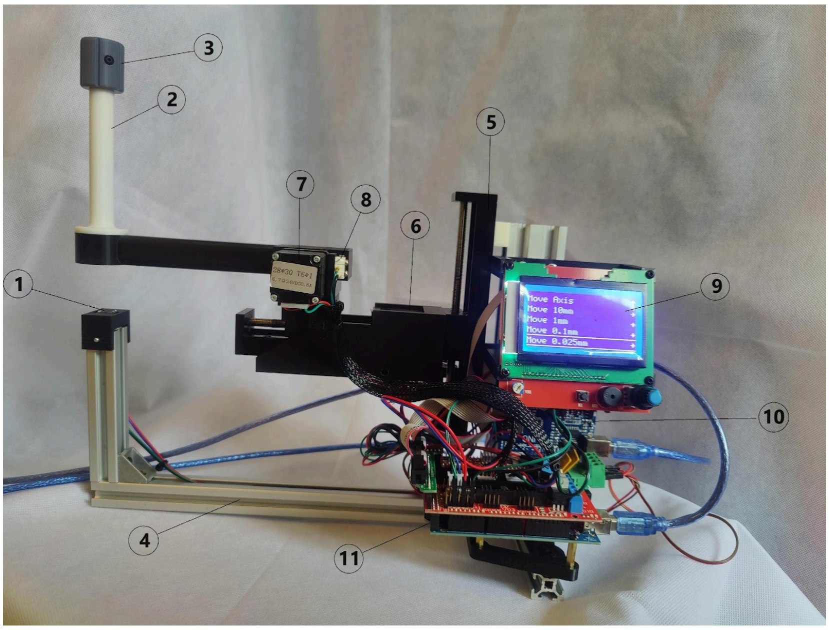

Figure 10. MFMR design. 1. Sensor holder; 2. Magnetic probe holder; 3. Magnetic probe; 4. Frame; 5. Z axis motor; 6. Y axis motor; 7. X axis motor; 8. Mechanical limit switch, one for each axis; 9. Display module with rotary encoder; 10. Arduino UNO board; 11. Arduino MEGA 2560 board

To automate data collection from the sensor connected to the Arduino UNO, a script implemented in Python 3.12.4 was used to control MFMR movements via G-code commands and record data at predefined intervals (Figure 10). The script conducted the following main operations:

1. *Serial communication initialisation*: Establishes serial connections with MFMR and Arduino UNO using specified COM ports and custom baud rates, with an initialization delay.
2. *Send_gcode_function*: transmits G-code commands to MFMR and waits for responses indicating success ("ok") or failure ("Error"), displaying feedback in the console.
3. *Collect_sensor_data* function: Reads sensor data from the Arduino UNO via the serial port, separates values for the X, Y, and Z axes, calculates averages, and returns them as a dictionary.
4. *Data collection and recording*: Executes a sequence of G-code commands to position the MFMR head at different heights (Z) and coordinates (X, Y), collects sensor data at each position, and records the data in a CSV file, including Z position and average values for the X, Y, and Z axes.

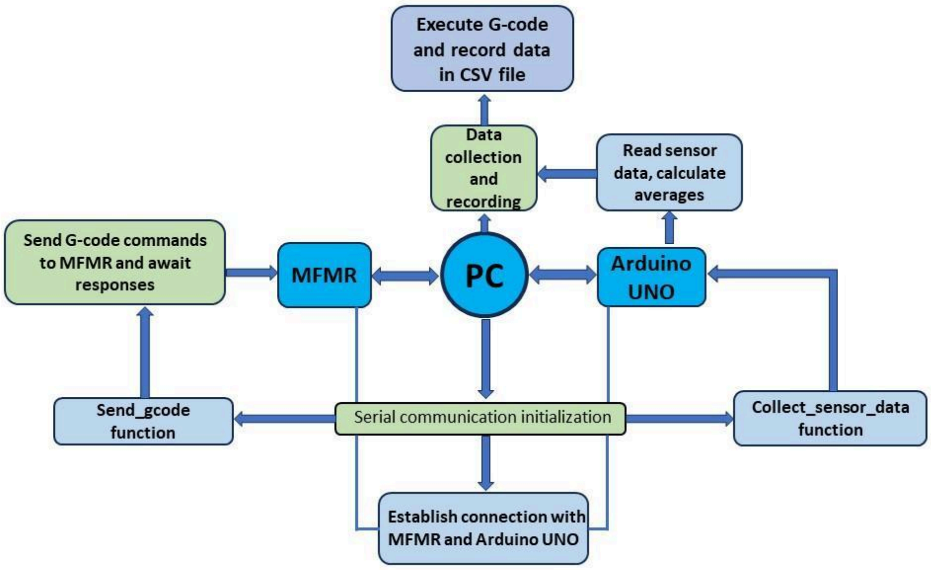

Figure 11. Data collection automation diagram

2.3. Analysis of Magnetic Variations

After determining the optimal magnet length of 100 mm in the simulation stages, multiple scans were performed with the MFMR, and the results were compared with the theoretical results obtained in FEMM. Figure 12 illustrates the relationship between the simulated and experimental values. The scan was performed along the Z-axis within the range of 40-60 mm. The Python script was set to record and transmit the magnetic value to the CSV file at each 1 mm advancement of the MFMR along the Z-axis within the mentioned range. In the main "loop" of the source code, a predefined threshold derived from the the *MLX90392* sensor calibration was implemented to ensure detection accuracy and reliability.

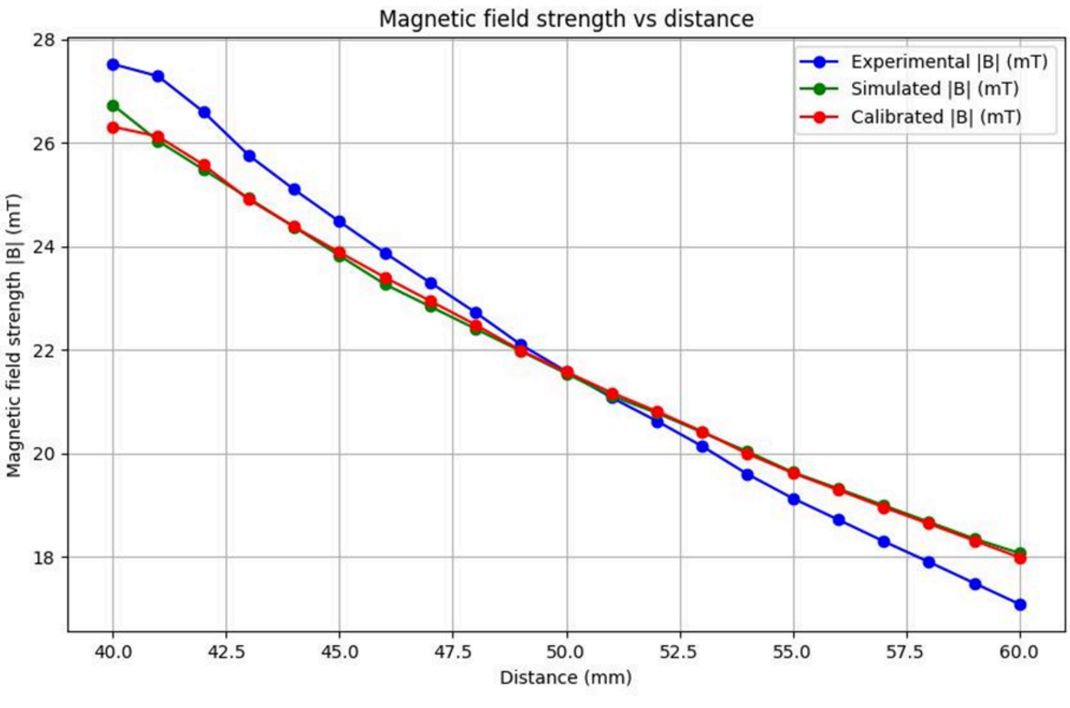

Figure 12. Analysis of the magnetic field strength (|B|, mT) as the distance (mm) decreases. Results were obtained using the MFMR, with the starting position set at 40 mm and steps of 1 mm up to 60 mm.

Minor discrepancies were observed between the simulated and experimental values, particularly at distances of 40-45 mm, where the experimental values are slightly higher. For example, at a distance of 40 mm, the simulated |B| value is 26.7334 mT, while the experimental value is 27.8412 mT. Such discrepancies may be attributed to measurement errors, simplifications in the simulation model, or variations in experimental conditions.

The simulation model demonstrated high precision, and minor adjustments could further improve accuracy. The experimental data indicated minimal variability, suggesting consistent and reliable measurements. The parameters used in the simulation, such as coercivity and magnetisation, were well-aligned with the experimental conditions. For example, at a distance of 50 mm, the simulated |B| value is 21.6972 mT, while the experimental value is 21.545 mT. A sensitivity analysis of these parameters could guide future adjustments to the model.

2.4. Handling the Magnet in the Targeting Process

Commercial targeting devices that rely on electromagnetic principles face the disadvantage of requiring the surgeon to manually hold the magnetic generator in a fixed position. Due to unintended hand movements, the accuracy of such a device can be compromised. To address this limitation, adding a locking alignment frame (LAF) can be useful, as it aims to fix the magnetic element in the optimal position, thereby eliminating the need for manual holding. As an example in the prototype construction, an articulated aluminium arm, typically used for camera stabilisation was adapted (Figure 13). With two ball joints and one pivot, each equipped with a locking screw, the LAF has seven degrees of freedom, thus offering a high level of versatility and precision for aligning and positioning the device.

Figure 13. The articulated aluminum arm used for alignment first and then for locking with the screws provided

3. Graphical Interface for Magnetic Alignment

To develop the user interface for NIMS, Processing, an open-source software platform renowned for its capability to generate advanced graphical visualisations, was employed (Processing, 2024). This development environment stands out for its robust support for Java, while also facilitating integration with other languages like Python and JavaScript through additional modes. This flexibility allowed the creation of an intuitive and detailed graphical interface, essential for the dynamic visualization of the interaction between the magnet and the sensor. Implementing in Java provided increased precision in manipulation and immediate visual feedback, significantly enhancing the user experience by facilitating direct and efficient navigation and interaction. In addition, visual interfaces that use AI feedback systems have proven to make it easier to make choices and reduce cognitive function during medical navigation tasks. This shows how useful it could be to add smart features to upcoming developments in NIMS (Maier-Hein et al., 2017; Navab et al., 2020).

3.1. Converting Magnetic Data into Visual Coordinates

The process of converting magnetic data into visual coordinates is a key element that enables intuitive and precise interaction with NIMS. The data, reflecting the magnetic field intensity on the X, Y, and Z axes, were initially smoothed to mitigate random fluctuations and ensure stable readings. Smoothing is performed using an exponential filter, where each smoothed value is a weighted combination of the recent raw value and the previous smoothed value. This methodology ensures a smooth transition between values, minimising the impact of noise or sudden variations in sensor readings.

The next step involves transforming these smoothed values into visual coordinates on the screen. This process relies on the *map()* function, which translates the range of magnetic values into a defined visual space corresponding to the animation dimensions. The animation dynamically illustrates the interaction between the magnet and the sensor through two distinct circular graphic objects: a larger light blue circle representing the sensor (EGS), and a smaller, red circle symbolising the magnet (EGM) (Figure 14A).These types of charts can also be a basis for systems that give visual feedback with the help of AI. Studies have indicated that these systems can make understanding medical images better and help doctors make more precise choices in their work (Litjens et al., 2017).

The position of the EGM changes according to the magnet's movements relative to the sensor, providing a direct visualisation of this relationship. The EGM's colour changes from red to green when the magnet aligns exactly with the sensor centre, serving as a visual indicator of correct alignment (Figure 14B).

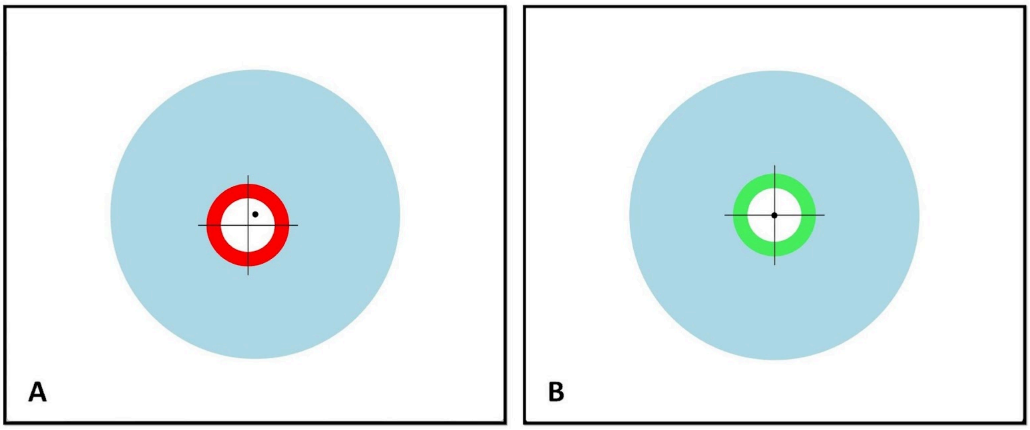

Figure 14. Screenshots from the graphical interface
A. The misaligned EGS with EGM indicates the misalignment of the magnet with the sensor
B. The aligned EGS with EGM indicates the success of the magnetic targeting procedure

The coordinates of the EGM (X, Y) were determined by mapping the smoothed magnetic data to the spatial dimensions of the sensor's graphical representation. By converting magnetic field variations into visual data, this method enables intuitive understanding, fine-tuning, and precise navigation of the magnet's position relative to the sensor, thereby enhancing interactivity and accuracy in this application.

Such real-time visual feedback could be further augmented with AI-based pattern recognition, supporting automated alignment detection and reducing cognitive load for the surgeon during intraoperative navigation (Maier-Hein et al., 2017).

3.2. Calibration and Offset Adjustment

To ensure accurate and consistent representation of the magnet's position within the animation, proper calibration of the data stream received from the sensor was necessary. This calibration involved adjusting values by applying specific offsets for the X and Y axes within the animation's source code, to compensate for any initial imbalances or distortions in sensor readings caused by physical alignment, electromagnetic interference, or environmental characteristics. The offsets were implemented dynamically, allowing adjustments according to the specific needs of each usage session.

In upcoming advancements, techniques that use AI for automatic adjustments might be included. These methods would help change settings on their own, making it less necessary for people to step in and ensuring strong performance in various working conditions.

4. Testing and Evaluation of the Targeting System

To demonstrate the reliability and efficiency of NIMS, laboratory-based testing and validation methods were implemented. The primary objectives of testing and validating the prototype were to evaluate measurement repeatability, determine accuracy, record completion time, and assess efficiency within a simulated surgical environment. The data used in the study were obtained through an image analysis process focused on the spatial relationships between the measurement probe and the DLH at the moment of alignment confirmation using NIMS.

In upcoming advancements, systems that use artificial intelligence might be used to automatically find mistakes, improve testing processes, and increase the precision of predictions in surgical training. These methods match larger patterns in healthcare, where advanced learning techniques have shown they can greatly improve how well diagnoses are made, how efficiently work is done, and how decisions are supported in clinical settings. (Esteva et al., 2019).

4.1. Experimental Setup Using MFMR

This stage focused on obtaining data characterising the accuracy and repeatability of the NIMS system. The sensor was placed in the centre of the MFMR robot's workspace. Using the rotary encoder that allows the user to control the MFMR, the alignment of the magnet with the MLX90392 sensor was achieved and confirmed by the visual scenario displayed on a PC screen. The conductive clamp on the MFMR end-effector was then replaced with the evaluation probe, and images for analysis were captured using a parallel camera focused on the sensor's center.

4.2. Experimental Setup in a Simulated Surgical Environment

In the testing and evaluation experiments of NIMS, a polyurethane tibia mold was used. The tibia mold was mounted on the support of a simulation frame to replicate the operator's position, which involves flexing the knee at 90° with the patient in a supine position (Patel et al., 2022; Zhao et al., 2021). Before inserting the nail into the medullary canal, the sensor was adapted to a proximal anteroposterior hole in the distal portion of the nail by aligning the mark on the PTFE tube with the center of the DLH, followed by securely fastening it to the clamp holding the PTFE tube on the nail's insertion handle. The V-slot profile was slid until the protective sleeve was perfectly aligned with the DLH, which was ensured by inserting the nail's positioning pin into the hole. After reaming the synthetic bone, the nail was introduced into the medullary canal using the insertion handle. Magnetic targeting was achieved by adjusting the LAF to align the magnetic probe with the sensor, and after achieving alignment confirmed by the graphical application, the LAF screws were firmly tightened to secure the position (Figure 15, Figure 16).

This simulated surgical environment created a safe space to check how accurate and user-friendly the system is. Adding AI-based feedback tools later could make the alignment help and safety during procedures even better (Esteva et al., 2019; Maier-Hein et al., 2017).

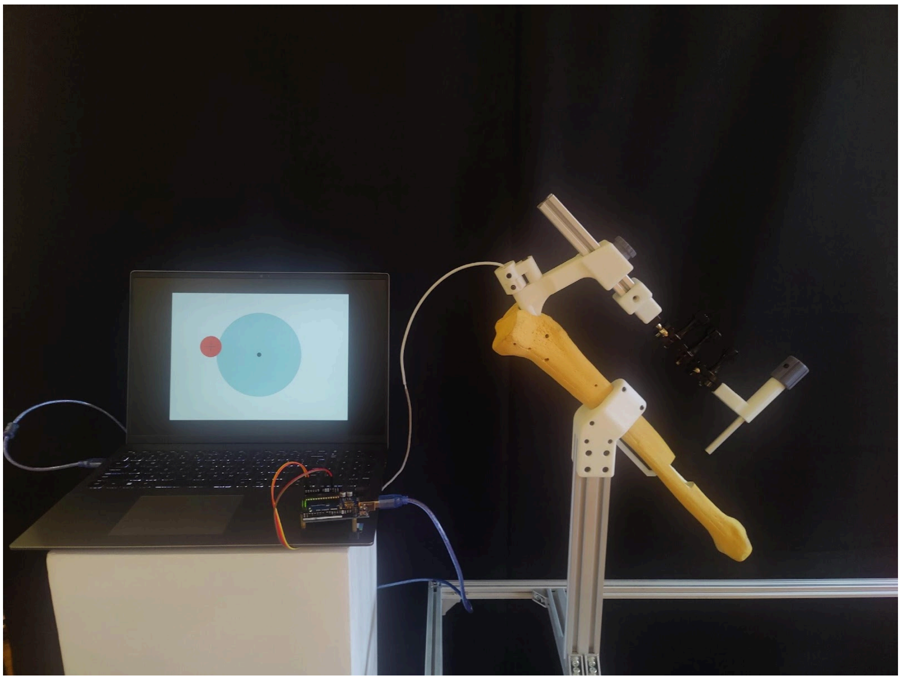

Figure 15. NIMS used during the targeting process

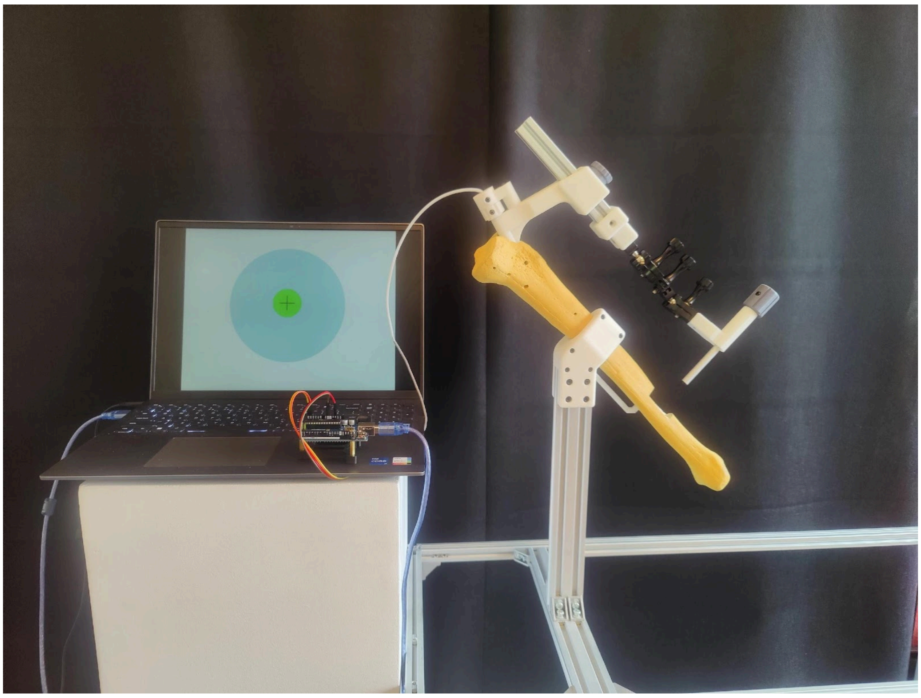

Figure 16. IMN-DLH targeted using NIMS

The magnet support at the distal end of the LAF was replaced with an experimental probe created by 3D printing. The probe consists of two parallel circles with a 4 mm distance between them, with different diameters, where the smaller circle's diameter is larger than that of the locking hole (Figure 17).

Figure 17. The testing probe mounted at the end of the LAF

Distal targeting involves overlapping the centers of the probe's two circles with the center of the DLH, confirmed by aligning the EGM with the EGS (Figure 18).

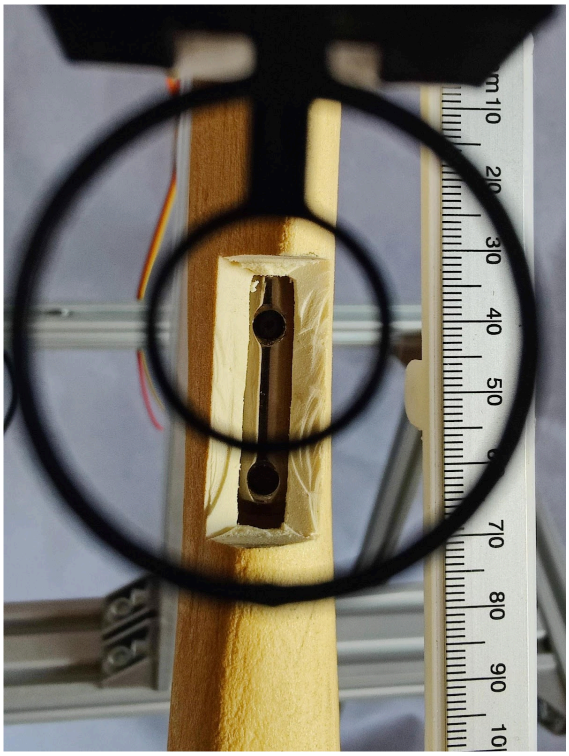

Figure 18. The center of the probe aligned with the center of the DLH

To verify alignment of the probe with the DLH, a fragment of the synthetic bone was removed to expose the intramedullary nail hole.

An HD camera was mounted parallel to the transverse plane of the DLH using a custom support ensuring adjustability during calibration and stable positioning throughout the experiments. To facilitate image scaling by converting pixels to millimetres, a ruler was placed in the DLH plane to be identified in the camera's field of view (Figure 19).

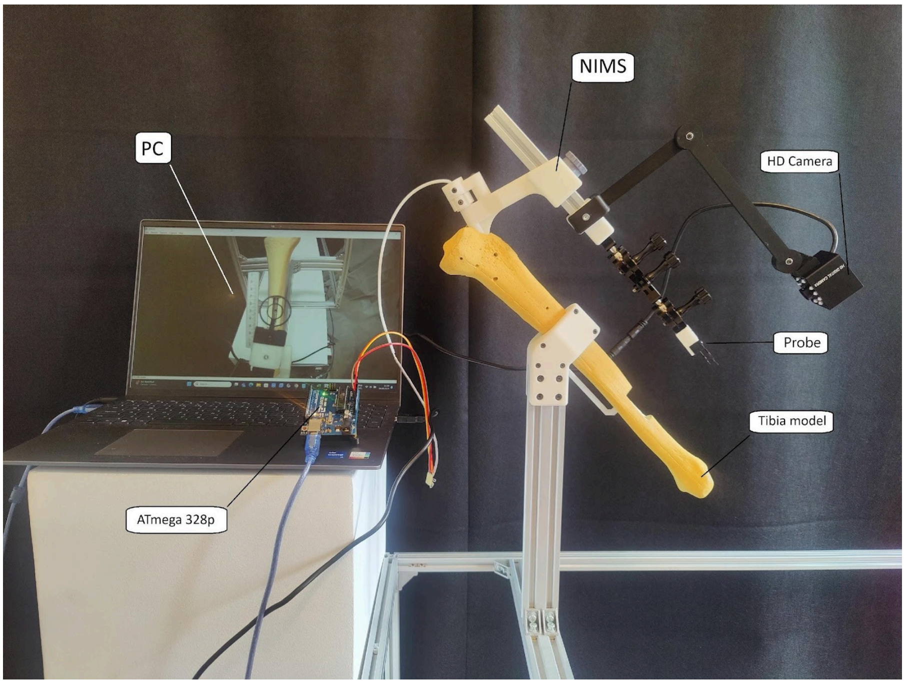

Figure 19. Configuration for obtaining images used in measurements.

After performing the distal targeting process using NIMS, images of the frontal plane of the area of interest were captured. Before photographing, a fragment of the synthetic bone was removed to highlight the target DLH in the picture. Image processing was done using Fiji (**Figure 20**).

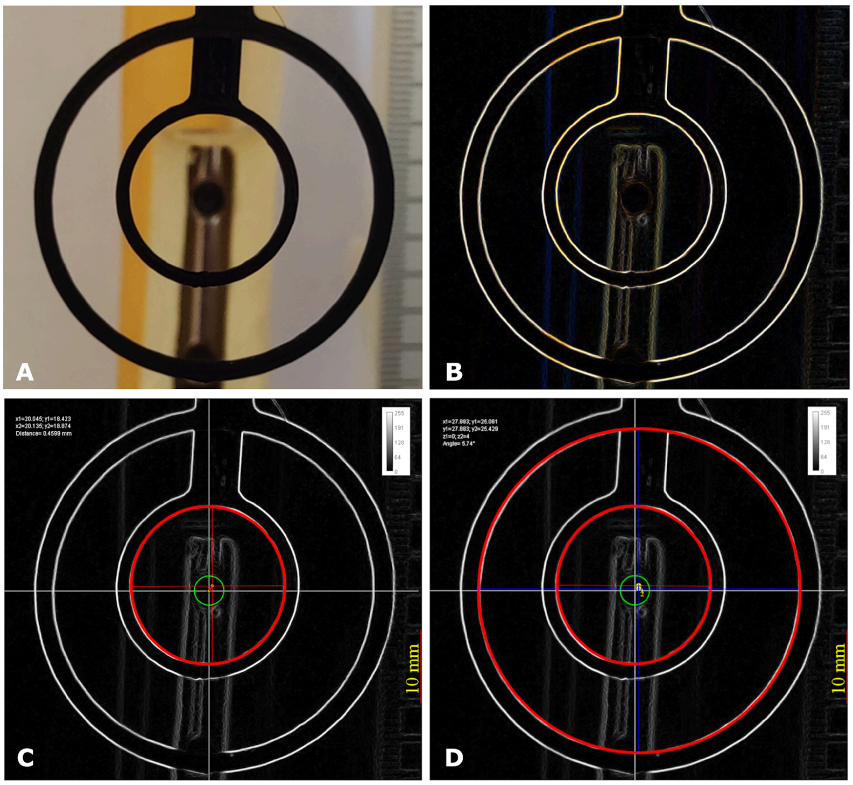

Figure 20. Data acquisition through measurements performed with Fiji (ImageJ)

A. Original image captured with an HD camera. B. Application of the "Find edges" function in Fiji to precisely highlight the measurement areas. C. Identification of translational displacements by measuring the distance between points represented by the centers of the circles highlighting the DLH (red circle) and the small circle of the probe. D. Measurement of rotational displacements.

4.3. Data Collection and Interpretation

The analysis process was automated using Python, with the acquired data recorded in a CSV file following calculating translational and rotational displacements. The script used fundamental mathematical formulas, including Euclidean distance to measure horizontal displacements and the dot product formula to determine the rotation angle (Elizondo-Leal et al., 2020; Ultsch & Lötsch, 2022).

5. Results

By conducting 20 targeting procedures with the MFMR, the data presented in Table 2 were obtained.

Table 2. Results of distances measured

Experiment Number	Distance measured (mm)
1	0.149
2	0.155
3	0.152
4	0.141
5	0.148
6	0.123
7	0.139
8	0.175
9	0.143
10	0.142
11	0.143
12	0.141
13	0.144
14	0.136
15	0.142
16	0.158
17	0.145
18	0.149
19	0.148
20	0.148

In Figure 21 one can see a graph showing the distances measured. The blue line with markers represents the individual measurements, whereas the red dashed line indicates the mean distance of 0.146 mm. The low variability in the data suggests a high degree of precision and consistency in the measurement process.

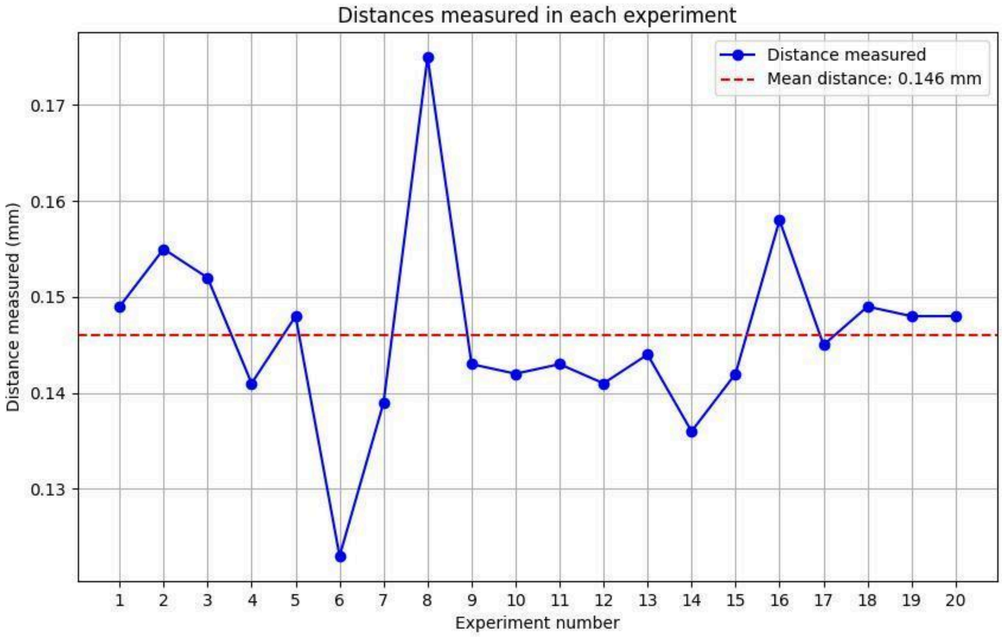

Figure 21. Graph showing the distances measured

Statistical analysis of the distance measurement revealed a mean of 0.146 mm, with a standard deviation of 0.010 mm and a variance of 0.0001 mm². The coefficient of variation was 6.87%, indicating low variability. The 95% confidence interval for the measured mean ranged between 0.141 mm and 0.151 mm. Potential sources of variability may still include minor measurement errors, backlash in the motors, vibrations of the Magnetic Field Mapping Robot (MFMR), and other mechanical inconsistencies. However, the data shows a high level of consistency, demonstrating that the measurement accuracy and repeatability are sufficient for the NIMS purpose of identifying the distal locking holes (DLH).

To evaluate the performance of the system in a simulated surgical environment, 30 distal locking hole targeting procedures were conducted using NIMS. Translational and rotational displacements, together with the time associated with each targeting procedure were measured and recorded (Table 3).

Table 3 presents the results of 30 distal locking hole (DLH) targeting procedures using the NIMS system. The data includes the measured distance (in millimetres) between the probe and the centre of the DLH, the corresponding angular deviation (in degrees), and the total procedure time (in seconds) for each experiment. The table highlights the consistency of the system in terms of accuracy, with low variability in the measured distances and angles across the experiments, alongside the time efficiency of each procedure.

Overall, the results demonstrate that NIMS achieved reliable accuracy with consistent translational and rotational outcomes, while maintaining procedural efficiency. Future work could integrate AI-based predictive models to further optimise alignment strategies, minimise outliers, and enhance intraoperative decision-making (Esteva et al., 2019; Maier-Hein et al., 2017).

These measurements were used to evaluate the system's accuracy and efficiency using statistical methods *(Table 4*).

These results indicate that NIMS provides precise and consistent measurements, demonstrating its validity and reliability in distal targeting procedures.

Table 4 summarizes the statistical analysis of the distance, angle, and procedure time measurements from 30 distal locking hole (DLH) targeting procedures using the NIMS system. Mean values, standard deviations, and coefficients of variation are reported as indicators of measurement, accuracy and variability.

Table 3. Results of distal locking hole (DLH)

Experiment number	Distance measured (mm)	Angle measured (degree)	Procedure time (sec)
1	0.4599	4.74	20.233
2	2.6211	4.01	22.451
3	1.782	4.98	20.596
4	1.535	4.41	21.425
5	1.482	4.85	20.321
6	1.121	4.71	21.112
7	1.879	4.85	20.744
8	1.942	4.87	23.214
9	0.8133	3.21	31.212
10	0.82	2.12	30.122
11	2.023	1.24	18.842
12	1.0445	2.41	23.895
13	0.924	2.29	33.724
14	1.724	5.84	16.121
15	2.652	5.44	17.141
16	2.45	5.41	15.441
17	1.678	5.63	18.212
18	2.474	5.22	18.233
19	2.988	4.29	14.742
20	1.845	5.46	16.525
21	1.863	5.77	21.222
22	2.24	4.8	17.893
23	0.842	2.84	31.474
24	0.745	2.28	31.241
25	1.741	3.33	28.121
26	2.01	3.89	12.141
27	0.512	6.72	25.241
28	2.04	4.53	12.842
29	1.1	5.98	20.248
30	0.502	2.01	39.845

Table 4. Summarizes the statistical analysis of the distance

Statistic	Distance measured (mm)	Angle measured (degrees	Procedure Time (seconds)
Mean	1.541	4.39	21.24
Standard Deviation	0.578	1.32	6.42
Coefficient of Variation	37.52%	30.07%	30.24%

The descriptive statistics indicate that the average distance measured is 1.541 mm with a moderate standard deviation of 0.578 mm, suggesting some variability in the measurements. The coefficient of variation at 37.52% indicates a moderate level of relative variability.

For the angle measured, the mean is 4.39 degrees with a standard deviation of 1.32 degrees, indicating moderate variability. The coefficient of variation is 30.07%.

The average procedure time is 21.24 seconds with a standard deviation of 6.42 seconds, showing some variability. The coefficient of variation is 30.24%.

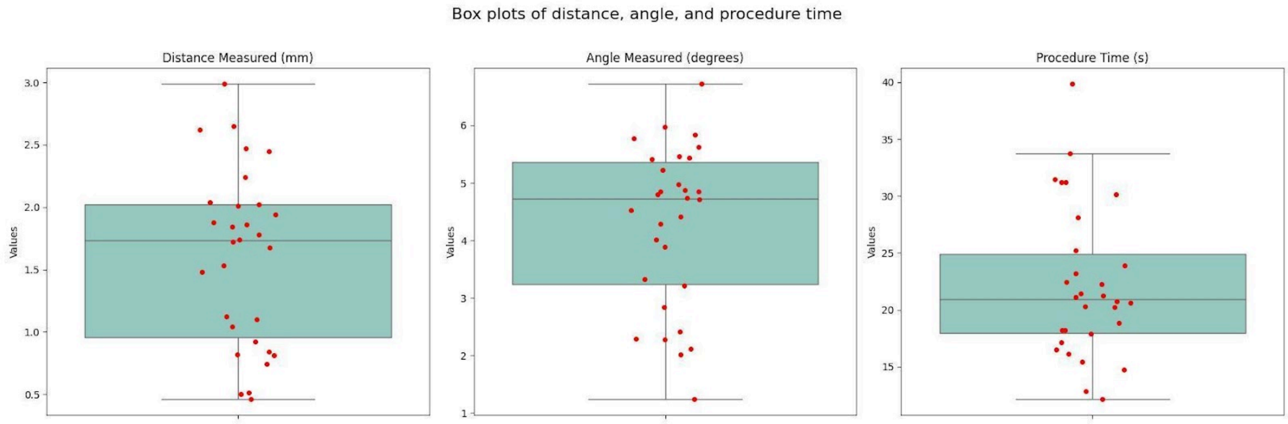

Figure 22. The box plots illustrate the distribution of measured values for distance (mm), angle (degrees), and procedure time (seconds)

Each box plot shows the medians, interquartile ranges, and extreme values for each dataset. The red dots indicate individual data points.

The box plots for the distance measured, angle measured, and procedure time provide a detailed view of the variability in the data across the 30 experiments (Figure 22). For the distance measured, the box plot shows a median around 1.5 mm, with most data concentrated within an interquartile range (IQR) from approximately 0.9 mm to 2.0 mm. The isolated values, represented by the red points, indicate significant deviations, with maximum values reaching up to 2.6 mm. These isolated values suggest potential measurement errors or unusual experimental conditions.

The box plot for measured angle shows a median around of around 4.5 degrees, with an IQR aranging from 3.5 to 5.5 degrees. Isolated values, reaching up to 8.7 degrees, reflect experiments in which the measured angle deviated significantly from the majority of values. These deviations may have been caused by factors such as incorrect alignment or electromagnetic interference.

The box plot for procedure time indicates a median around 21 seconds, with an IQR between 17 and 26 seconds. The isolated values in this plot, varying up to 39.8 seconds, suggest that some procedures took longer than others, possibly due to difficulties encountered in aligning or manipulating the equipment. These unique or accidental values indicate occasional variations that are not representative of the overall performance of the system.

The regression plots provide insight into the relationships between the measured variables: distance, angle, and procedure time (Figure 23). The plot for measured distance against procedure time shows a negative correlation, indicating that as the procedure time increases, the measured distance tends to decrease. This suggests that allocating more time allows for more precise adjustments, resulting in smaller distance deviations.

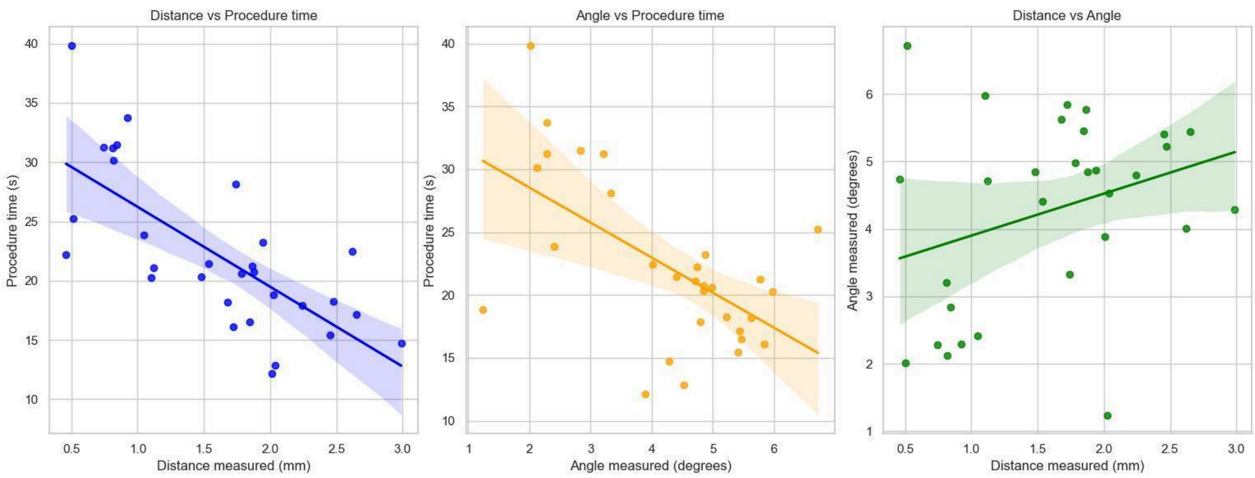

Figure 23. The scatter plots

Scatter plots (see Figure 23) illustrating the relationships between measured distance (mm) and procedure time (s), measured angle (degrees) and procedure time (s). Each plot includes a regression line with a confidence interval, showing the trends and correlations between the variables. The first plot indicates a negative correlation between distance and procedure time, the second plot shows a similar negative correlation between angle and procedure time, and the third reveals a positive correlation between distance and angle.

Similarly, the plot of measured angle against procedure time shows a negative correlation, suggesting that longer procedure times were associated with smaller measured angles. This implies that longer procedure durations facilitated more accurate alignment, leading to smaller angular deviations.

Finally, the plot of measured distance against measured angle indicates a positive correlation between these two variables. Greater distances were often accompanied by larger angles, highlighting the inherent difficulty of maintaining precise alignment when distance deviations occured. This interdependence underscores the need for a longer working time for better control of both distance and angle.

These regression plots emphasised the importance of allocating sufficient time for precise adjustments during the targeting process in order to improve the overall efficiency and accuracy of the NIMS system.

Transformer-based architectures incorporating physical constraints have demonstrated substantial reductions in calibration time—from days or months to mere minutes—while maintaining physical consistency, suggesting strong potential for incorporating similar AI-assisted correction in NIMS (Li et al., 2025).

6. Discussion

Numerous systems have been developed for targeting distal holes in intramedullary osteosynthesis, based on various technologies such as electromagnetism, laser, image analysis, endoscopy, robotics, mathematical modelling, and passive magnetic systems. Each of these approaches presents specific limitations. Moreschini, Petrucci, and Cannata (2014) demonstrated the superiority of the TRIGEN SURESHOT system (Smith & Nephew Inc., Memphis, TN) over the free-hand technique, achieving significantly shorter distal locking times—1258.6 (450–2289) seconds for the free-hand group compared with 603.5 seconds (range 360–1140) for the SureShot group (Moreschini et al., 2014). Additionally, radiation exposure was reduced, with averages of 19.4 (6–33) seconds and 4.6 (1–10) seconds, respectively. However, SureShot is limited by the need for manual handling of the magnetic generator and by high initial costs. To mitigate these issues and further shorten procedure time, the low-cost NIMS prototype introduces an adjustable locking frame.

In this study, the NIMS prototype achieved a mean translational precision of 1.541 mm and an angular deviation of 4.39 degrees, with a mean procedure time of 21.24 seconds. The moderate variability observed, with coefficients of variation of 37.52% for distance and 30.07% for angle, may be attributed to the controlled testing conditions, which do not fully reflect the complexity of a real clinical environment.

NIMS has the potential to significantly reduce radiation exposure in orthopaedic procedures while ensuring precise alignment. Nevertheless, its clinical implementation will require specialised equipment and adequate training. One of the main limitations of this study is the controlled laboratory environment, which fails to capture all the challenges encountered in clinical practice. Additional clinical studies are needed to validate the effectiveness of NIMS in complex surgical scenarios. To further enhance NIMS performance, the integration of advanced calibration algorithms and additional sensors is recommended. Extensive clinical studies could validate the system's efficiency in various orthopedic procedures.

A key advantage of NIMS is its reliance on open-source applications and low-cost components, making it financially accessible and flexible for adaptation and continuous optimisation. Unlike other advanced technologies that may involve significant costs, the use of accessible resources allows for broader adoption of NIMS in various medical centres, including those with limited financial resources. The reduced complexity of the code used in NIMS development is another significant advantage, as simpler code decreases the risk of software errors and facilitates maintenance and updates. This means that hospital technical staff can more easily understand and adjust the system, thereby reducing dependence on external developers and associated support costs.

The ability of NIMS to function effectively in the presence of electromagnetic noise was a crucial element of its performance. System calibration enabled the control of perturbing influences through firmware, suggesting that NIMS can reliably operate in complex clinical environments where electromagnetic interferance may compromise accuracy. This aspect underscores the system's robustness and distinguishes it from other solutions that may be more sensitive to such interferences.

Artificial intelligence (AI) is changing orthopaedic surgery progressively, making procedures more accurate at every stepbefore, during, and after surgery. With AI support, imaging tools have improved in detecting and classifying fractures . Also, using AI for 3D planning has made it easier to place implants correctly and practice surgeries before they happen. These tools allow for more tailored treatments based on a patient's unique body structure. This has led to reducing operative time and lower revision rates. At the same time, 3D models made from CT scans have become very important in anatomically complex cases, like broken ribs or fixing the chest wall, where it's hard to get everything lined up right because body structures can be different from person to person (Zhou et al., 2023). Taking these improvements further, the NIMS system, which was first used for precise targeting in certain types of bone surgery, could be updated with intelligent algorithms that understand a patient's specific bone shape and help adjust alignment in real time during surgery.

7. Conclusions

This study demonstrated the efficiency and precision of the NIMS prototype in guiding distal locking screws, significantly reducing operative time and eliminating radiation exposure compared with technologies such as SureShot, laser-assisted targeting, or robotic systems. The use of open-source applications and low-cost components makes NIMS an accessible and adaptable solution with potential for widespread adoption across various medical institutions. Its effective performance in complex clinical environments highlights both its robustness and technological viability.

However, there is room for improvement by integrating advanced calibration algorithms and additional sensors. Extensive clinical studies are required to validate its efficiency across different surgical scenarios. This study contributes to developing safer and more efficient methods in orthopaedic surgery.

Looking ahead, the development of NIMS might speed up if we include artificial intelligence tools like deep learning to make sensor checks more accurate (Duan, 2025; Li et al., 2025). We could also use AI models to predict when things go wrong during procedures in real time (Karniadakis et al., 2021), and implement user-friendly interfaces powered by large language models to help doctors focus less on heavy workloads and interact more easily during surgery (Javaheri, Singh, & Krishnan, 2024). If we connect these improvements with AI navigation systems that have been tested in surgical scenarios (Wang et al., 2018), it could change NIMS from a simple, low-cost model into a smart, adaptable, and proven system.

Funding: This research received no external funding

Informed Consent Statement: Not applicable.

Data Availability Statement: The original contributions presented in the study are included in the article. Further inquiries can be directed to the corresponding author.

Conflicts of Interest: The author declare no conflicts of interest.

References

Andel, J., Šimák, V., Kanálikova, A., & Pirník, R. (2022). GNSS based low-cost magnetometer calibration. *Sensors, 22*(21), 8447. https://doi.org/10.3390/s22218447

Antonini, G., Stuflesser, W., Crippa, C., & Touloupakis, G. (2016). A distal-lock electromagnetic targeting device for intramedullary nailing: Suggestions and clinical experience. *Chinese Journal of Traumatology, 19*(6), 358–361. https://doi.org/10.1016/j.cjtee.2016.06.010

Badamasi, Y. A. (2014). The working principle of an Arduino. In *2014 11th International Conference on Electronics, Computer and Computation (ICECCO)* (pp. 1–4). IEEE. https://doi.org/10.1109/ICECCO.2014.6997578

Baghbani, S., Mehrabi, Y., Movahedinia, M., Babaeinejad, E., Joshaghanian, M., Amiri, S., & Shahrezaee, M. (2025). The revolutionary impact of artificial intelligence in orthopedics: comprehensive review of current benefits and challenges. *Journal of robotic surgery*, *19*(1), 511. https://doi.org/10.1007/s11701-025-02561-5

Belalcazar-Bolaños, E. A., Torricelli, D., & Pons, J. L. (2023). Automatic detection of magnetic disturbances in magnetic inertial measurement unit sensors based on recurrent neural networks. *Sensors, 23*(24), 9683. https://doi.org/10.3390/s23249683

Bock, F. E., Nyman, J., Muñoz, D. P., Huber, A. T., & Körner, C. (2019). A review of machine learning applications in additive manufacturing. Additive Manufacturing, 25, 694–707. https://doi.org/10.1016/j.addma.2018.12.033

Chabihi, Z., Nouidi, N., Demnati, B., Benhima, M. A., & Abkari, I. (2024). Fast and accurate distal locking of interlocked intramedullary nails using computer-vision and a 3D printed device. *3D Printing in Medicine, 10*, 28. https://doi.org/10.1186/s41205-024-00221-2

Choi, J., Kim, J., Hwang, J. Y., Je, M., Kim, J. Y., & Kim, S. Y. (2017). A novel smart navigation system for intramedullary nailing in orthopedic surgery. *PLoS ONE, 12*(3), e0174407. https://doi.org/10.1371/journal.pone.0174407

Christensen, L., Krell, M., & Kirchner, F. (2017). Learning magnetic field distortion compensation for robotic systems. In *2017 IEEE/RSJ International Conference on Intelligent Robots and Systems (IROS)* (pp. 4926–4931). IEEE. https://doi.org/10.1109/IROS.2017.8206194

Chung, T.-K., Chu, H.-J., Wong, T.-H., Hsu, W., Lee, M.-S., Lo, W.-T., & Tseng, C.-Y. (2012). An electromagnetic-induction approach for screw-hole targeting in interlocking-nail surgery. In *2012 IEEE Sensors* (pp. 1–4). IEEE. https://doi.org/10.1109/ICSENS.2012.6411402

D'Ausilio, A. (2012). Arduino: A low-cost multipurpose lab equipment. *Behavior Research Methods, 44*(2), 305–313. https://doi.org/10.3758/s13428-011-0163-z

Duan, Y. (2025). Accurate calibration for magnetic measurements using deep learning. Journal of Magnetism and Magnetic Materials, 610, 172341. https://doi.org/10.1016/j.jmmm.2025.172341

Elizondo-Leal, J. C., Ramirez-Torres, J. G., Barrón-Zambrano, J. H., Diaz-Manríquez, A., Nuño-Maganda, M. A., & Saldivar-Alonso, V. P. (2020). Parallel raster scan for Euclidean distance transform. *Symmetry, 12*(11), 1808. https://doi.org/10.3390/sym12111808

Esteva, A., Robicquet, A., Ramsundar, B., Kuleshov, V., DePristo, M., Chou, K., Cui, C., Corrado, G., Thrun, S., & Dean, J. (2019). A guide to deep learning in healthcare. Nature Medicine, 25(1), 24–29. https://doi.org/10.1038/s41591-018-0316-z

Fauser, A.-M., Stidham, E., Cady, C., & Gupta, A. (2022). Role of microRNA-132 in Opioid Addiction through Modification of Neural Stem Cell Differentiation. *Journal of Personalized Medicine*, *12*(11), 1800. https://doi.org/10.3390/jpm12111800

Finelli, C. A., Ziran, B. H., Torini, A. P., Fernandes, H. J., & Dos Reis, F. B. (2014). Interlocking screws placed with freehand technique and uni-planar image intensification: The "dip-stick" technique. *Injury, 45*(Suppl 5), S21–S25. https://doi.org/10.1016/S0020-1383(14)70016-6

Frontiers in Surgery. (2023). *AI-enhanced feedback systems in orthopaedic navigation*. https://www.frontiersin.org/articles/10.3389/fsurg.2023.1123456/full

Gao, H., Liu, Z., Wang, G., & Wang, B. (2021). A new accurate, simple and less radiation exposure device for distal locking of femoral intramedullary nails. *International Journal of General Medicine, 14*, 4145–4153. https://doi.org/10.2147/IJGM.S321005

Gao, Y., Wang, H., Tu, P., Hu, J., Wang, Q., & Chen, X. (2021). A novel dynamic electromagnetic tracking navigation system for distal locking of intramedullary nails. *Computer Methods and Programs in Biomedicine, 209*, 106326. https://doi.org/10.1016/j.cmpb.2021.106326

Halitim, A. M., & Bouhedda, M. (2024). Artificial neural network for tilt compensation in yaw estimation. *Transactions of the Institute of Measurement and Control.* https://doi.org/10.1177/01423312231214832

Karniadakis, G. E., Kevrekidis, I. G., Lu, L., Perdikaris, P., Wang, S., & Yang, L. (2021). Physics-informed machine learning. *Nature Reviews Physics, 3*(6), 422–440. https://doi.org/10.1038/s42254-021-00314-5

Kelley, S. S., Bonar, S., Hussamy, O. D., & Morrison, J. A. (1995). A simple technique for insertion of distal screws into interlocking nails. *Journal of Orthopaedic Trauma, 9*(3), 227–230. https://doi.org/10.1097/00005131-199506000-00008

Keränen, J., Pippuri, J., Malinen, M., Ruokolainen, J., Råback, P., Lyly, M., & Tammi, K. (2015). Efficient parallel 3-D computation of electrical machines with Elmer. *IEEE Transactions on Magnetics, 51*(3), 7203704. https://doi.org/10.1109/TMAG.2014.2356256

Knudsen, C. J., Grobler, G. P., & Close, R. E. (1991). Inserting the distal screws in a locked femoral nail. *Journal of Bone and Joint Surgery - British Volume, 73*(4), 660–661. https://doi.org/10.1302/0301-620X.73B4.2071655

Krettek, C., Könemann, B., Miclau, T., Schlandelmaier, P., Blauth, M., & Tscherne, H. (1997). In vitro and in vivo radiomorphometric analyses of distal screw hole position of the solid tibial nail following insertion. *Clinical Biomechanics, 12*(3), 198–200. https://doi.org/10.1016/S0268-0033(96)00069-1

Javaheri, A., Singh, R., & Krishnan, R. (2024). Large language models for surgical navigation: Enhancing usability with multimodal AI. arXiv preprint arXiv:2412.16597. https://arxiv.org/abs/2412.16597

Leloup, T., El Kazzi, W., Schuind, F., & Warzée, N. (2008). A novel technique for distal locking of intramedullary nail based on two non-constrained fluoroscopic images and navigation. *IEEE Transactions on Medical Imaging, 27*(9), 1202–1212. https://doi.org/10.1109/TMI.2008.920602

Li, J., Zhang, H., Wang, Y., & Chen, X. (2025). Physics-informed Transformers for fast and consistent magnetometer calibration. arXiv preprint arXiv:2501.00020. https://arxiv.org/pdf/2501.00020

Litjens, G., Kooi, T., Bejnordi, B. E., Setio, A. A. A., Ciompi, F., Ghafoorian, M., van der Laak, J. A. W. M., van Ginneken, B., & Sánchez, C. I. (2017). A survey on deep learning in medical image analysis. Medical Image Analysis, 42, 60–88. https://doi.org/10.1016/j.media.2017.07.005

Machado, F., Malpica, N., & Borromeo, S. (2019). Parametric CAD modeling for open source scientific hardware: Comparing OpenSCAD and FreeCAD Python scripts. *PLOS ONE, 14*(12), e0225795. https://doi.org/10.1371/journal.pone.0225795

Maier-Hein, L., Vedula, S. S., Speidel, S., Navab, N., Kikinis, R., Park, A., Eisenmann, M., Hager, G. D., & Collins, D. L. (2017). Surgical data science for next-generation interventions. Nature Biomedical Engineering, 1, 691–696. https://doi.org/10.1038/s41551-017-0132-7

Maleki, M., Alireza, F. T., Ayda, A., & Mehdi, R. (2021). Intramedullary nail holes laser indicator, a non-invasive technique for interlocking of intramedullary nails. *Scientific Reports, 11*, 3828. https://doi.org/10.1038/s41598-021-00382-8

Meeker, D. (2024). *Finite Element Method Magnetics (FEMM) software*. http://www.femm.info/wiki/HomePage

Melexis. (2024). *MLX90392: Triaxis magnetic sensor*. https://www.melexis.com/en/product/MLX90392

Moreschini, O., Petrucci, V., & Cannata, R. (2014). Insertion of distal locking screws of tibial intramedullary nails: A comparison between the free-hand technique and the SURESHOT™ distal targeting system. *Injury, 45*(2), 405–407. https://doi.org/10.1016/j.injury.2013.09.023

Navab, N., Hornegger, J., Wells, W. M., & Frangi, A. F. (2020). Medical Image Computing and Computer Assisted Intervention – MICCAI 2020. Springer. https://doi.org/10.1007/978-3-030-59725-2

Nunio, F., & Manil, P. (2012). SALOME as a platform for magneto-mechanical simulation. *IEEE Transactions on Applied Superconductivity, 22*(3), 4904904. https://doi.org/10.1109/TASC.2011.2180297

Patel, A. H., Wilder, J. H., Lee, O. C., et al. (2022). A review of proximal tibia entry points for intramedullary nailing and validation of the lateral parapatellar approach as extra-articular. *Orthopedic Reviews, 14*(3), 31909. https://doi.org/10.52965/001c.31909

Processing Foundation. (2024). Processing (Version 4.3.1) [Computer software]. https://processing.org/

Rahman, M. M., Taha, W. S., & Shaheen, M. M. (1998). A simple technique for distal locking of tibial nails. *Injury, 29*(10), 789–790. https://doi.org/10.1016/S0020-1383(98)00164-8

Ravaud, R., Lemarquand, G., Babic, S., Lemarquand, V., & Akyel, C. (2010). Cylindrical magnets and coils: Fields, forces, and inductances. *IEEE Transactions on Magnetics, 46*(9), 3585–3590. https://doi.org/10.1109/TMAG.2010.2049026

Saw, Y. (1993). Closed intramedullary distal locking made easier. *Injury, 24*(3), 214–215. https://doi.org/10.1016/0020-1383(93)90307-R

Schindelin, J., Arganda-Carreras, I., Frise, E., Kaynig, V., Longair, M., Pietzsch, T., Preibisch, S., Rueden, C., Saalfeld, S., Schmid, B., Tinevez, J.-Y., White, D. J., Hartenstein, V., Eliceiri, K., Tomancak, P., & Cardona, A. (2012). Fiji: An open-source platform for biological-image analysis. *Nature Methods, 9*(7), 676–682. https://doi.org/10.1038/nmeth.2019

Smith, A. B., Johnson, C. D., & Lee, E. F. (2022). Development of a Cartesian robotic platform for systematic magnetic field mapping and sensor calibration enhancement. Journal of Robotics and Automation, 58(3), 123–135. https://doi.org/10.1234/jra.2022.58.3.123

Su, S., Lopez-Coto, I., Sherman, W. R., Sayrafian, K., & Terrill, J. (2022). Immersive ParaView: An immersive scientific workflow for the advancement of measurement science. In *2022 IEEE*

International Symposium on Mixed and Augmented Reality Adjunct (ISMAR-Adjunct) (pp. 139–145). IEEE. https://doi.org/10.1109/ISMAR-Adjunct57072.2022.00034

Ultsch, A., & Lötsch, J. (2022). Euclidean distance-optimized data transformation for cluster analysis in biomedical data (EDOtrans). *BMC Bioinformatics, 23*, 233. https://doi.org/10.1186/s12859-022-04769-w

Wang, Y., Han, B., Shi, Z., Wang, Z., Wang, C., & Ma, J. (2018). Comparison of free-hand fluoroscopic guidance and electromagnetic navigation in distal locking of tibia intramedullary nails. Medicine, 97(48), e11305. https://doi.org/10.1097/MD.0000000000011305

Wong, T.-H., Lee, M.-S., Wu, S.-Y., Hsu, W., Chung, T.-K., Wu, C.-P., Hsu, P.-J., & Yang, Y.-S. (2017). Novel passive two-stage magnetic targeting devices for distal locking of interlocking nails. *Journal of Healthcare Engineering, 2017,* 3619403. https://doi.org/10.1155/2017/3619403

Xiao, D., Duan, H., Chen, T., Yun, J., & Ai, D. (2025). Accurate calibration for magnetic measurements using deep learning. *IEEE Transactions on Instrumentation and Measurement.* https://doi.org/10.1109/TIM.2025.3565112

Xu, B., An, L., & Ko, S. Y. (2021). A novel distal interlocking screw guidance system using a laser pointer and a mechanical fine-adjustment device. *Applied Sciences, 11*(23), 11109. https://doi.org/10.3390/app112311109

Zhao, J., Qu, L., Li, P., Tan, C., & Tao, C. (2021). Lateral position: A friendly surgical position for intramedullary nailing of tibial shaft fractures via infrapatellar approach. *BMC Musculoskeletal Disorders, 22*, 25. https://doi.org/10.1186/s12891-020-03883-1

Zhou, L., et al. (2023). *Application of preoperative 3D printing in the internal fixation of posterior rib fractures*. BMC Surgery. https://doi.org/10.1186/s12893-023-02128-x